A Guidance and Control Law Design for Precision Automatic Take-off and Landing of Fixed-Wing UAVs

Dong Il, You[1], Yeon Deuk, Jung[1], Sung Wook, Cho[1],
Hee Min, Shin[1], Sang Hyup, Lee[1] and David Hyunchul Shim[2]

KAIST, Daejeon, South Korea

This paper presents an automatic take-off and landing control system (ATOLS) for fixed-wing UAVs. We propose a guidance and control system to satisfy the requirement for high-precision landing using arresting wires. For trajectory tracking, Line-of-Sight (LOS)-based longitudinal and lateral guidance laws are derived. For the design of inner loop controllers, linear models are identified directly from the flight data. In order to maintain the consistency of the control performance in the presence of flight regime changes during take-off and landing, the linear baseline controller is augmented with a compensator designed using $\mathcal{L}_1$ adaptive control theory, which eliminates the need for conventional gain scheduling. The proposed control system is implemented on a scale Cessna UAV with an arresting hook for validation. The proposed take-off and landing system demonstrated a consistent performance in a series of test flight on a full-scale carrier model.

Nomenclature

X, Y, Z	=	axis in local Cartesian coordinate
x, y, H	=	horizontal positions and altitude of vehicle
ϕ, θ, γ	=	roll, pitch angles (Euler angles) and vertical flight path angle
$\psi_{course}, \psi_{path}, \psi_{LOS}$	=	heading angle of velocity vector, reference path and LOS command, respectively
g	=	gravitational acceleration
a_N, a_{cmd}	=	normal and command accelerations in vehicle body axis, respectively
L_{app}, H_{app}	=	lateral and vertical approach length, respectively
P_e, H_e	=	lateral and altitude errors with respect to reference path, respectively
V_t	=	total velocity of vehicle
R_{min}	=	minimum turn radius of vehicle

I. Introduction

According to the automation level defined by the Defense Advanced Research Projects Agency (DARPA), a majority of recent Unmanned Aerial Vehicles(UAVs) correspond to Level 2 or a state where attitude stabilization and guided navigation technology have become stable enough to carry out real operational missions[1]. DARPA recommends future UAVs to reach Level 3 where the conventional burden of the mission placed on the ground pilot, such as take-off and landing, reconnaissance, and ground attack missions, is greatly reduced so that ground pilots can solely concentrate on the core mission and the supervision of a group of UAVs[1]. A majority of the currently operational UAVs are heavily dependent on external pilots due to the air traffic control and technological limitations

---

[1] Graduate Student Researcher, Dept. of Aerospace Engineering, 291 Daehakro, Yuseonggu, Daejeon, South Korea.
[2] Associate Professor, Dept. of Aerospace Engineering, Yuseonggu, Daejeon, South Korea, Senior Member.

in take-off and landing procedure. The accident statistics of UAVs operated by the U.S. Army, Navy, and Air Force reveal that approximately 50% of all UAV accidents are attributed to human factors[2]. Also, according to the same reference, the portion of accidents caused during landing is relatively large due to the difficulty to control the vehicle manually under adverse weather conditions with limited situational awareness. For civilian aviation, instrument landing system(ILS) has been very successful but it is available only in larger airports and to aircraft equipped with appropriate VHF receivers. Recently, a number of automatic landing methods using GPS(Global Positioning System), MLS(Microwave Landing System), and IBLS(Integrity Beacon Landing System) have been proposed[3-5]. Among these, GPS-based navigation has been recognized as the key enabling technology for next generation aviation due to the higher precision than current ground-based landing aides such as VOR/DME or ILS and its availability over the whole world.

Figure 1. Developed automatic take-off and landing system for manned / unmanned aircraft (USA, Global Hawk(Left), F/A-18E/F (Center), X-47B(Right))

Automatic take-off and landing technology have been tested using various manned and unmanned vehicles such as the Global Hawk, F/A-18E/F, and X-31. These technologies have been applied to UAVs currently in development and are predicted to greatly improve the operability of the UAV[6-8]. Keeping up with the current state-of-the-art research and development of UAV flight control, we consider operation scenarios where the UAV automatically takes off from a runway and lands at a desired touchdown point. Particularly, we are interested in the high-precision automatic take-off and landing system for aircraft carrier landing. The carrier deck landing requires a highly accurate touchdown control to grasp one of the arresting wires on the very short landing zone. In order to meet the requirements, reference paths for take-off and landing phases are first designed and LOS-based longitudinal and lateral path tracking guidance laws are proposed. The proposed lateral guidance law is designed based on vehicle kinematics. For the design of inner loop controllers, linear models are identified using the flight data. In order to minimize the control performance variation due to the trim state change caused by flap deployment, power setting and vehicle speed during take-off and landing, a compensator is designed using $\mathcal{L}_1$ adaptive control theory, which eliminates the need for conventional gain scheduling approach. Also, an operational logic of landing and take-off is implemented to handle the emergency situations including go-around and bouncing. These designed algorithms and operational logics were tested and evaluated in PILS(Processor-In-the-Loop Simulation) using MATLAB/Simulink with an X-Plane simulator. The proposed system were finally validated in a series of flight experiments using a mock-up full-size carrier deck with arresting wires and demonstrated a consistent performance sufficient for carrier deck landing as well as conventional landing on runways.

This paper is organized as follows. In Section II, the automatic take-off and landing system design is introduced. In this section, lateral path following LOS guidance based on vehicle kinematics and longitudinal LOS guidance law is described. Also, the system identification, baseline controller and $\mathcal{L}_1$ adaptive controller are presented. In Section III, the flight experiment results are presented and discussed. In Section IV, the conclusion is given.

II.   Automatic Take-off and Landing System Design

A. Testbed and System Requirements

The UAV used in this study is a typical fixed-wing airplane with tricycle landing gear configuration as shown in Figure 2. The airplane is a scaled Cessna 172, which is controlled by ailerons, flaps, elevators, a rudder and a steerable nose gear. The airplane is modified to have a deployable arresting hook for cable-assisted precision landing. Table 2 shows the detailed specifications of the UAV.
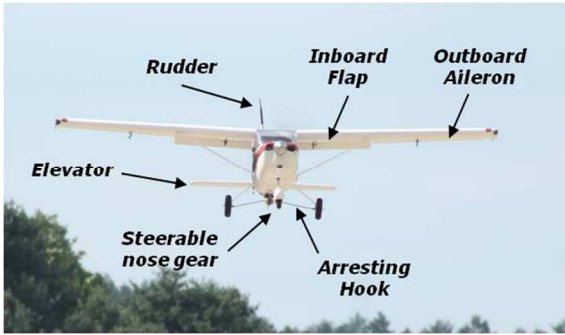
American Institute of Aeronautics and Astronautics

Figure 2. UAV Testbed for landing experiment

Table 1. UAV specifications.

Wing Span	2745mm
Length	2145mm
Cruise speed	12~40 m/s
Endurance	25 min
G.T.O.W	13.5kg
Wing Loading	139.0 dm^2
Power System	DC Brushless Motor, Lithium-Polymer Battery

In this study, we consider a scenario where a UAV take-offs from a runway and performs a precision landing on a desired touchdown point as illustrated in Figure 3.
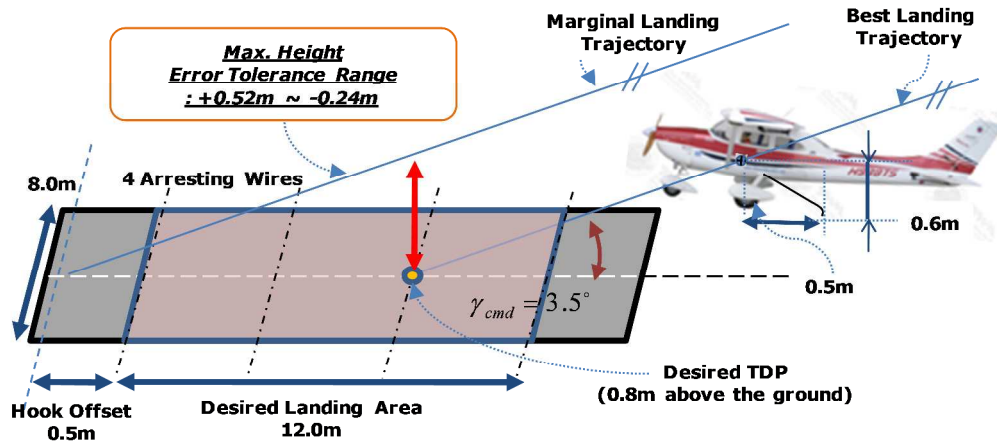

Figure 3. Landing requirement geometry

The desired landing zone is where four arresting wires installed. Each wire is four meters apart and the desired landing area is eight meter wide. In the automatic landing sequence, the landing accuracy at the desired Touchdown Point (TDP) were set as follows.

Table 2. Precision landing requirements.

	Longitudinal	Lateral
Max. Tolerance	-0.24m~ +0.52m	4.0m

B. LOS based Lateral and Longitudinal Guidance Law

In this section, the guidance law using a LOS based algorithm for the tracking of the reference path is presented.
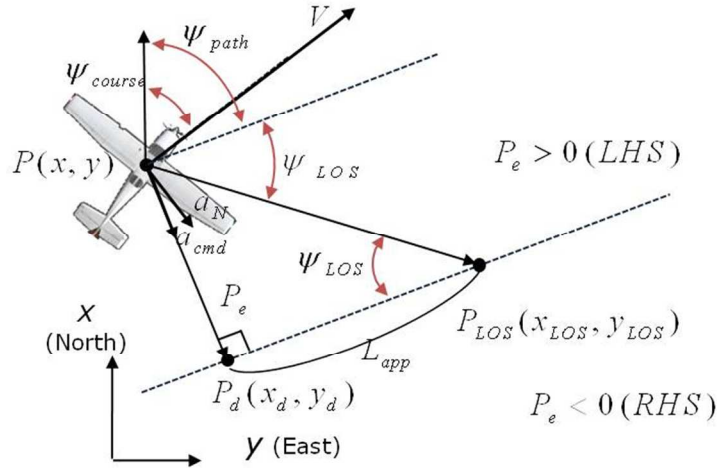

Figure 4. Lateral LOS guidance law

The lateral tracking algorithm allows for the tracking of virtual straight trajectory connecting the route[9]. When the current aircraft position is described as (x, y), the perpendicular position error P_e to the target position (x_d, y_d) along the runway extension and its first derivative can described by Eq.(1).

$$P_e = \begin{bmatrix} \sin\psi_{path} & -\cos\psi_{path} \end{bmatrix} \begin{bmatrix} x - x_d \\ y - y_d \end{bmatrix}$$

$$\dot{P}_e = V_t \sin\Delta\psi \, sgn(P_e)$$

(1)

where $\Delta\psi = \psi_{path} - \psi_{course}$.

In Eq.(1), when the aircraft lies to the left of the straight trajectory, the sign is positive. Likewise, when the aircraft lies to the right of the trajectory, the sign is negative. The LOS angle can be written as follows:

$$\psi_{LOS} = \tan^{-1}\left(\frac{K_{pl}P_e + K_{dl}\dot{P}_e}{L_{app}} \right)$$

$$\psi_{cmd} = \psi_{path} + \psi_{LOS}$$

(2)

These heading angles are related with a reference roll angle command for the inner-loop controller:

$$\phi_{cmd} = K_{yaw}(\psi_{cmd} - \psi_{course})$$

(3)

Here, when designing a LOS guidance law composed of design parameters such as the gains K_{pl}, K_{dl} and the approach length L_{app}, empirical or trial-and-error methods are generally used. However, these approaches do not guarantee a proper and consistent tracking performance. Also, the design parameters should be re-designed with vehicle operating conditions as vehicle maneuver limits and velocity. Therefore, a design method of a LOS guidance law based on vehicle kinematic model is proposed to determine the design parameters. The main idea in this approach is to consider vehicle velocity and minimum turn radius of the vehicle when the airplane is assumed to be in a steady wing level or steady sustained turn condition on a horizontal plane.

4

American Institute of Aeronautics and Astronautics

As can be seen in Figure 4, a_{cmd} is the acceleration command perpendicular to the given linear path. g and a_N denote gravity acceleration and normal acceleration with respect to velocity vector of the vehicle, respectively. The normal acceleration can be expressed as

$$a_N = g \tan \phi \tag{4}$$

a_{cmd}, the command value to minimize the lateral perpendicular position error P_e, can be described by Eq.(5) using a second-order linear point-mass model.

$$a_{cmd} = \omega_n^2 P_e + 2\zeta \omega_n \dot{P}_e \tag{5}$$

In Eq.(5), there always exist real positive values of natural frequency ω_n and damping ratio ζ to stabilize the linear model exponentially. The guidance law designed in this way is able to guarantee its convergence and stability.

Then, the roll command angle derived from a second-order linear model in Eq. (5) with normal acceleration in Eq.(4) is given in Eq.(6):

$$\phi_{cmd}^{acc} = \tan^{-1}\left(\frac{a_N}{g}\right) = \tan^{-1}\left(\frac{\omega_n^2 P_e + 2\zeta \omega_n \dot{P}_e}{g} \cdot \cos \Delta\psi\right) \tag{6}$$

The roll angle command calculated by Eq.(2) and (3) is represented as

$$\phi_{cmd}^{LOS} = K_{yaw} \cdot \tan^{-1}\left(\frac{K_{pl} P_e + K_{dl} \dot{P}_e}{L_{app}} + \Delta\psi\right) \tag{7}$$

For simplicity, with the conditions that K_{yaw} is one and heading error $\Delta\psi$ is zero, the roll command angles in Eq.(6) and Eq.(7) should be identical.

$$\phi_{cmd}^{acc} = \phi_{cmd}^{LOS} \tag{8}$$

$$\tan^{-1}\left(\frac{\omega_n^2 P_e + 2\zeta \omega_n \dot{P}_e}{g}\right) = \tan^{-1}\left(\frac{K_{pl} P_e + K_{dl} \dot{P}_e}{L_{app}}\right)$$

$$\frac{K_{pl}}{L_{app}} = \frac{\omega_n^2}{g} \ , \ \frac{K_{dl}}{L_{app}} = \frac{2\zeta \omega_n}{g} \tag{9}$$

Consequently, the relationship between the LOS gains and 2nd order linear model gains is derived by comparing each roll command angle.

So far, only the second-order model is considered for path tracking. The next step is to determine the natural frequency and damping ratio of linear model for determining of LOS gains. The minimum turn radius of vehicle is given as follows:

$$R_{min} = \frac{V_{t_{cmd}}^2}{g \tan \phi_{max}} \tag{10}$$

The geometry of the problem is shown in Figure 5. The solid line therein is a possible flight path to converge into the given linear path. At the point of inflection $P_{inflection}$, the acceleration command a_{cmd} should be zero because the normal acceleration has zero value while the heading error is not zero. Hence, the Eq.(5) can be rewritten as Eq.(11).
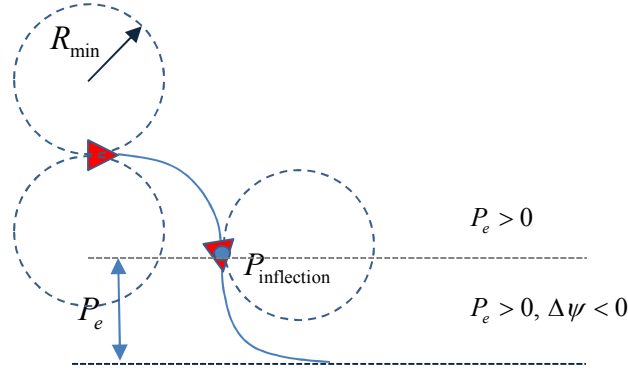
Figure 5. Lateral geometry

$$a_{cmd} = \omega_n^2 P_e + 2\zeta\omega_n \dot{P}_e = 0$$
$$\omega_n^2 P_e = -2\zeta\omega_n \dot{P}_e$$

(11)

Here, the vehicle located on the $P_{inflection}$ can converge into a given path with a maximum bank angle if the P_e is larger than the minimum turn radius of the vehicle. Using this condition, we obtain Eq.(12).

$$P_e = -\frac{2\zeta}{\omega_n} V_t \sin\Delta\psi \cdot \text{sgn}(P_e) \geq R_{min} = \frac{V_t^2}{g\tan\phi_{max}}$$
$$\omega_n \leq \frac{-2\zeta g \tan\phi_{max} \sin\Delta\psi \, \text{sgn}(P_e)}{V_t}$$

(12)

Using Eq.(12), the maximum value of ω_n can be determined where the heading error is $\pm 90°$.

$$\omega_n = \frac{2\zeta g \tan\phi_{max}}{V_t} \; where \; V_t \geq V_{stall}$$

(13)

As can be seen in Eq.(13), that ω_n is inversely proportional to the vehicle speed V_t and directly proportional to the bank angle limit ϕ_{max}. As a result, the design parameters are minimized from the K_p, K_d, L_{app} to ζ only and the gains depend on the vehicle speed and limits of bank angle.

In order to evaluate the roll angle tracking performance of the proposed algorithm, nonlinear simulations have been carried out using the kinematic model in Eq.(14) with three different combinations of initial heading, position error and roll time delay. The simulation runs using fourth-order Runge-Kutta method with 100Hz sampling frequency.

$$\dot{P}_e = V_t \sin\Delta\psi$$
$$\Delta\dot{\psi} = -\frac{g\tan\phi}{V_t}$$

(14)

First of all, the simulation is performed in the presence of various heading angle error and position. We assume that the vehicle has a constant velocity 20 m/s without any tracking delay. With forty degrees of the maximum bank angle limit, the minimum turn radius can be calculated as 48.6 meters.

Figure 6 shows the phase portrait of the LOS guidance law designed based on the proposed algorithm. The initial position of each trajectory is denoted by a circle. The red dashed line represents the flight trajectory that converges from the initial state to the final desired point at the origin. The blue line is the shortest path between two

points in a plane constrained by the initial and final orientation and maximum curvature of the path. It is the well-known Dubin's path that composed of minimum turn-radius curves and straight lines[10].

Based on this observation, the dashed line in Figure 6 shows that the LOS guidance law provides the shortest path to converge to the origin in case of the initial condition with 48.6m and -90 degree.
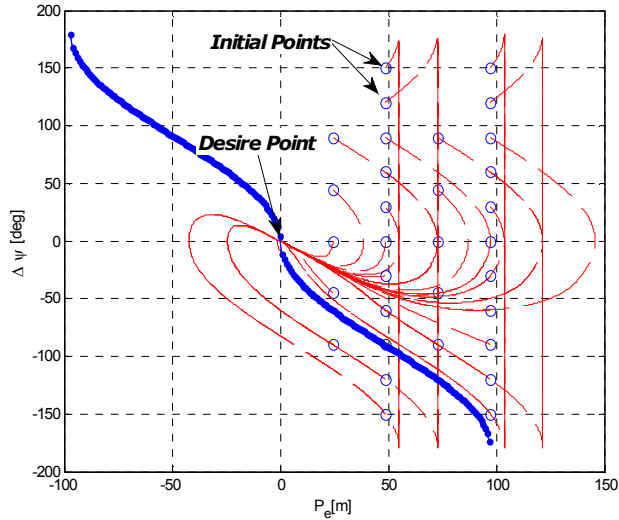

**Figure 6. Phase portrait**
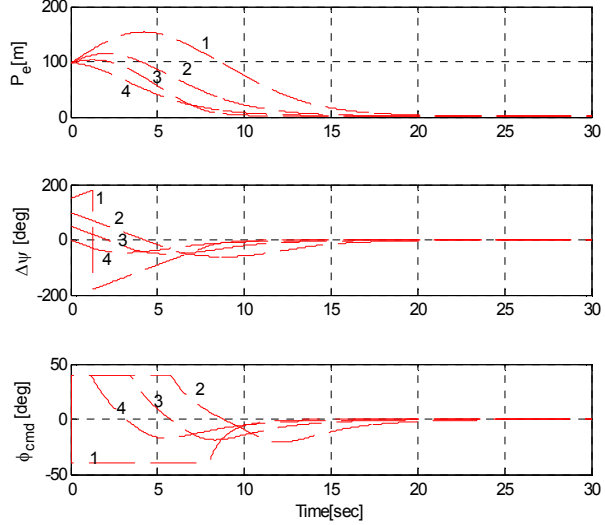
**Figure 7. Line path tracking history
(constant velocity condition)**

Figure 6 and 7 show the result of the simulation at the fixed position with different initial heading angle errors. Although the vehicle has large initial errors in position and heading angle, it can track the reference path without overshoot in the transient response.

Figure 8 shows that the LOS guidance law proposed above can consistently track the given path with varying vehicle speeds. This indicates that the guidance law can provide a reliable tracking performance during the take-off and landing phases.
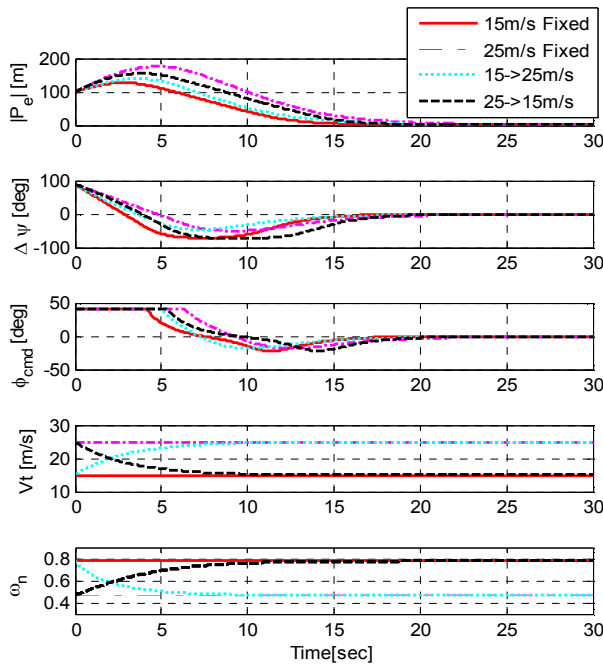
**Figure 8. Line path tracking history
(velocity variations condition)**
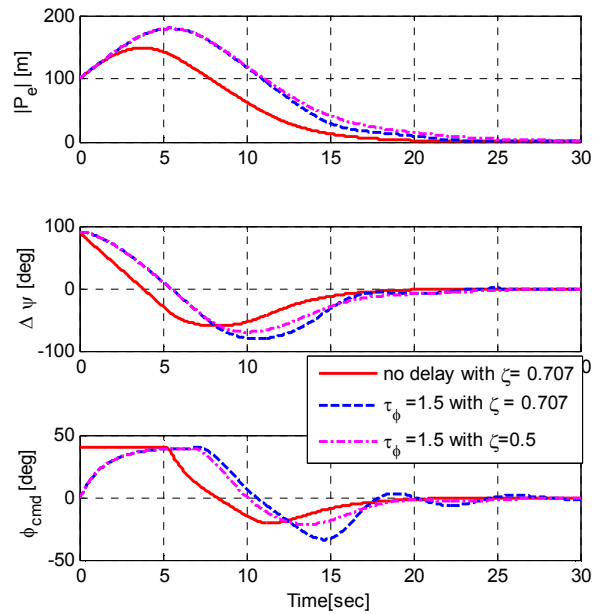
**Figure 9. Line path tracking history
(ζ changes with delay)**

7

American Institute of Aeronautics and Astronautics

Also, in order to analyze the effect of time delay in tracking, the vehicle is modeled as a first-order linear model with small time constant in roll maneuver. As can be seen in Figure 9, the tracking performance deteriorates as the roll time constant increases. Then, it is possible to tune the overall performance using only the damping ratio to suppress the undesirable ripple caused by large roll time delay. In summary, one can see that the proposed approach allows for an efficient design process of guidance law.

Likewise, Eq.(2) can be applied to the guidance law design in the longitudinal direction as shown in Figure 10. If γ_{path} is small, the vertical error ($H_e \cos \gamma_{path}$) with respect to the reference path can be approximated by altitude error(H_e) of the current altitude.

$$\gamma_{LOS} = \tan^{-1}\left(\frac{K_{ph}H_e + K_{ih}\int H_e}{H_{app}}\right)$$

(15)

$$\gamma_{cmd} = \gamma_{path} + \gamma_{LOS}$$

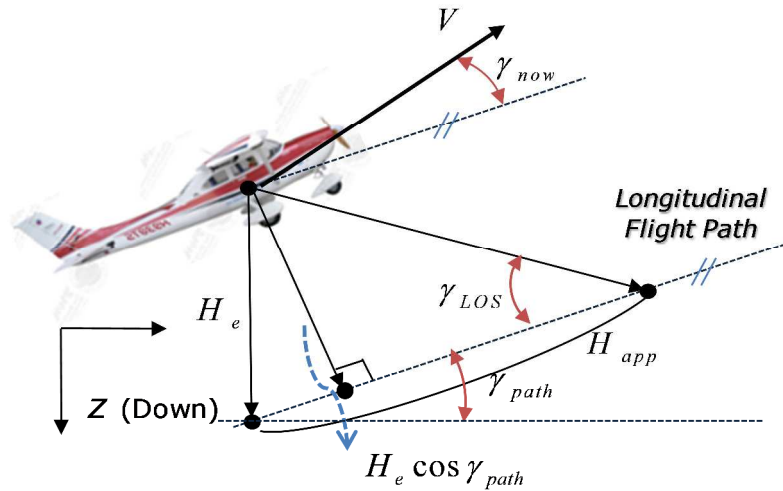where $H_e \cos \gamma_{path} \approx H_e = H_{cmd} - H_{now}$.

Figure 10. Longitudinal LOS guidance law

The flight path angle command needs to measure the angle of attack to control the pitch angle for tracking. However, since the testbed used in this study is not equipped with any angle of attack sensor, the integration term in Eq. (15) is included to compensate for the altitude error and track the altitude through the pitch angle control only. Therefore, Eq. (15) can be reorganized based on the trim state pitch angle.

$$\theta_{cmd} = \gamma_{path} + \gamma_{LOS} + \theta_{trim, Vt=15m/s}$$

(16)

In Eq. (16) , the γ_{path} is a feedforward term to improve the tracking performance. Here, K_{ph} and K_{ih} gains are determined using actual flight experiment results since there is no unique relationship between the pitch angle and altitude without knowing the exact value of angle of attack. Hence, a sufficient approach time and distance before touchdown is needed to allow the integrator term to converge to a trim value and compensate for the altitude error in the absence of angle of attack sensor.

The approach distance H_{app} is determined depending on the vehicle speed such that

$$H_{app} = K_{hv}V_t$$

(17)

American Institute of Aeronautics and Astronautics

C. System Identification and Baseline Attitude Controller Design

This section describes the aircraft modeling through system identification and the baseline controller design. Vehicle model identification using flight data is a widely adopted method for both fixed-wing and rotary-wing aircraft. In this study, the frequency sweep-like control input is injected to roll and pitch channels in turn and the vehicle response is recorded. The system identification algorithms find a number of candidate transfer functions to minimize the error between the actual and predicted system response.
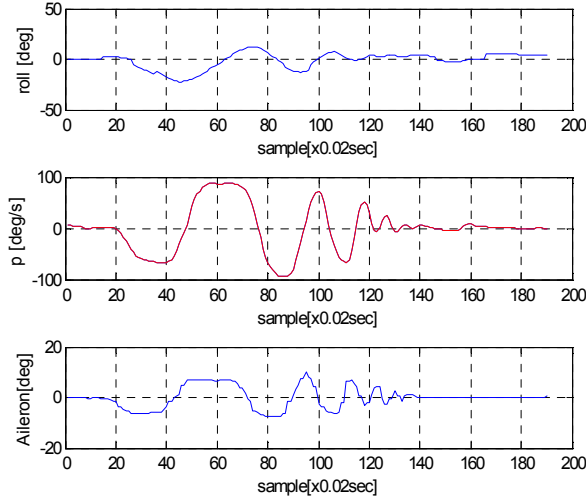
Figure 11. Roll response ID data
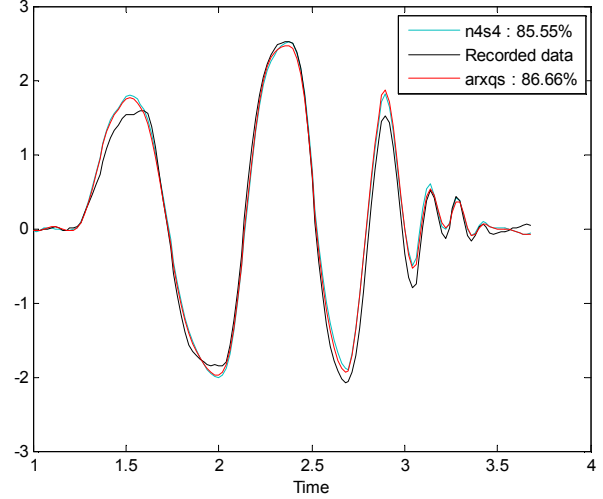
Figure 12. Roll model estimation result

Figure 11 shows the system response, roll rate and angle, to the aileron input exerted by the test pilot. The response of the aircraft was recorded at 50Hz. The system identification result using MATLAB System Identification Toolbox[TM] is given in Figure 12, which shows the predicted outputs by output error(n4s4) and autoregressive(arx) algorithms overlaid on the actual flight data. The detailed description of the system identification algorithm is given in the references[11-12]. We choose the candidate, among those with feasible pole/zero pairs, that has minimal prediction error. We also repeat a similar process to find the pitch axis model. The obtained models for roll and pitch dynamics are given as follows.

$$\frac{\phi}{\delta_{ail}} = \frac{0.039574(s-146)(s+140.6)(s^2+172.4s+2.27e4)}{s(s^2+51.07s+727)(s^2+54.68s+2075)} \tag{18}$$

$$\frac{\theta}{\delta_{elev}}(s) = \frac{-40.992(s-76.68)(s^2+13.43s+315.7)}{s(s^2+11s+238.2)(s^2+35.96s+586.7)} \tag{19}$$

9
American Institute of Aeronautics and Astronautics

Based on the results given above, each nominal PD attitude controller for roll and pitch channel was constructed.
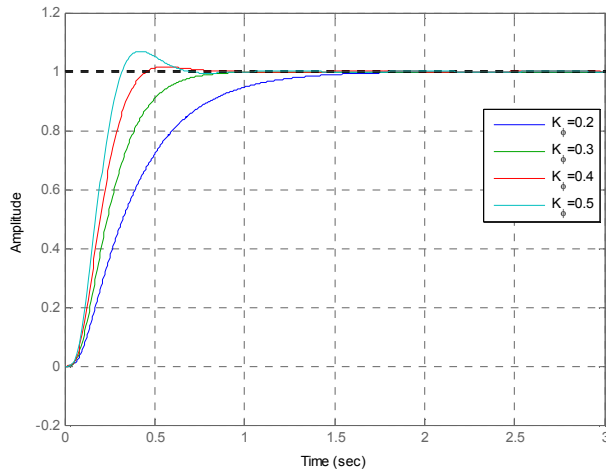

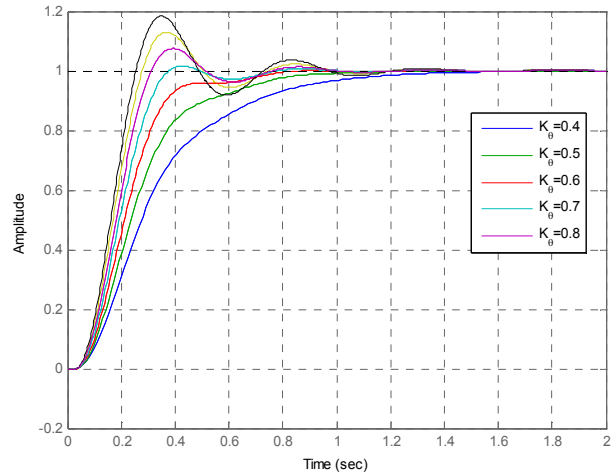**Figure 13. Step response feedback loop of roll model**

Figure 14. Step response feedback loop of pitch model

D. $\mathcal{L}_1$ Adaptive Output-Feedback Augmentation

In this section, the $\mathcal{L}_1$ adaptive control design for tracking of reference command is presented. The $\mathcal{L}_1$ adaptive control law is similar to the model reference adaptive control (MRAC) with a difference of including a low-pass filter in the feedback loop allows for the application of a large adaptation gain. Owing to this, $\mathcal{L}_1$ adaptive control guarantees good asymptotic tracking and transient performances simultaneously by suppressing high frequency adaptive control signals and allowing a convenient setting of appropriate adaptation gain values[13-14].

The $\mathcal{L}_1$ adaptive controller tracks the roll and pitch angle commands produced by the aforementioned guidance law while changing the command value produced by an outer loop to track the reference command value by acting similarly with the reference model desired by the closed-loop system including the inner loop controller.
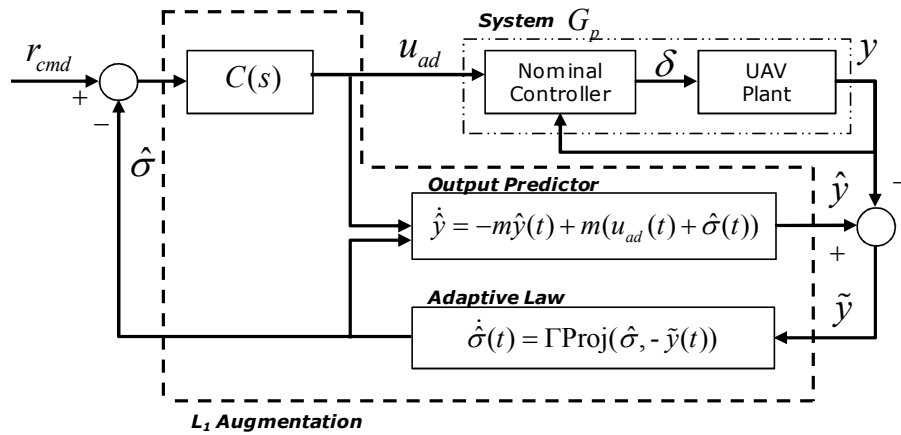

Figure 15. Closed-loop system with $\mathcal{L}_1$ adaptive controller

Since the linear roll and pitch models are identified using the flight data at a trim velocity of 15 m/s with retracted flap, they are bound to be inaccurate when the vehicle speed or flap setting change during landing and take-off. Thus, the $\mathcal{L}_1$ adaptive controller is introduced to handle the uncertainties of the plant, and define an adaptive control signal which compensates for these uncertainties. Here, for the sake of simplicity, the reference model is assumed to be a first-order model and the roll and pitch reference models are chosen as

American Institute of Aeronautics and Astronautics

$$y(s) \approx M_y(s)\, y_{cmd}(s) \ \text{ where } M_\bullet(s) = \frac{m_\bullet}{s + m_\bullet}, m_\bullet > 0 \tag{20}$$

In this study, the output feedback $\mathcal{L}_1$ adaptive controller is used and the whole control system structure is shown in Figure 15. In order to track the desired reference value where the output $\hat{y}(t)$ is bounded using the $\mathcal{L}_1$ adaptive controller, the following output predictor, adaptation law and control law is required. First, examining the output predictor, it can be described with Eq.(21).

$$\dot{\hat{y}}(t) = -m\hat{y}(t) + m(u_{ad}(t) + \hat{\sigma}(t)), \hat{y}(0) = y_0 \tag{21}$$

Here, m is the desired reference model, while $u_{ad}(t)$ and $\hat{\sigma}(t)$ are the adaptive input of the system and the adaptive estimate value, respectively. The adaptive estimate is defined in the following fashion due to the projection operator[14].

$$\dot{\hat{\sigma}}(t) = \Gamma \mathrm{Proj}(\hat{\sigma}, -\tilde{y}(t)) \tag{22}$$

Then, $\tilde{y}(t) = \hat{y}(t) - y(t)$ refers to the attitude error between output predictor and actual plant output. Based on this, the adaptive control law produces the adaptive control input as shown below.

$$u_{ad}(s) = C(s)(r(s) - \hat{\sigma}(s)) \tag{23}$$

Here, $r(s)$ refers to the bounded reference input and $C(s)$ is the strictly proper low-pass filler with a DC gain of 1. The choice of $C(s)$ defines the trade-off between performance and robustness[15]. In this study, an adaptive control system was constructed utilizing a first-order lowpass filter, and the adaptive control system composed of $M(s)$ and $C(s)$ that guarantees the stability of the closed-loop system shown in Eqs.(20)-(23) is shown below.

$$H(s) = \frac{G_p(s)M_y(s)}{C(s)G_p(s) + (1-C(s))M_y(s)} \tag{24}$$

The validity of the stability and guaranteed performance boundary values of the closed-loop reference system are given in the reference[14]. This adaptive control law designed above is integrated with the conventional inner-loop attitude controller as shown in Figure 15.

Figure 16 shows two vehicle responses with the conventional PD controller is activated with or without the $\mathcal{L}_1$ adaptive controller. In the longitudinal flight test, it can be observed that the reference command value is well tracked even with disturbances and when the center of gravity is shifted to aft. Similarly, the lateral response at the bottom of Figure 17 shows that the roll angle tracking error value due to disturbances are displaying improved characteristics compared to the conventional PD controller.

The $\mathcal{L}_1$ adaptive control method uses a large adaptive control gain for fast adaptation and a lowpass filter is used to prevent any performance degradation in the transient response characteristics. However, for actual implementation using a digital flight control computer, a practical challenge comes with the sampling interval in the discrete control system. While a larger adaptation gain tends to improve the performance in the continuous time domain, the same results in the opposite in discrete time domain due to the discretization of the low-pass filter and the projection operator, which prohibits using a comparably large adaptive control gain. Therefore, one should try to use faster sampling rate, which is limited by the capability of the flight computer.

In this study, the flight control computer is running on 50Hz frequency. With this setup, the flight test results showed that the adaptive gain of Eq. (22) had stable performances within 2.0 in both longitudinal and lateral directions. The pitch and roll adaptation gains was chosen to be 1.0 and 0.2, respectively. The pitch adaptation gain was designed relatively larger to cope with the trim position value change due to the flap deployed during the automatic take-off and landing. $\mathcal{L}_1$ adaptive controller also eliminates the need for additional gain scheduling as it can adeptly cope with the perturbed dynamics during the take-off and landing.
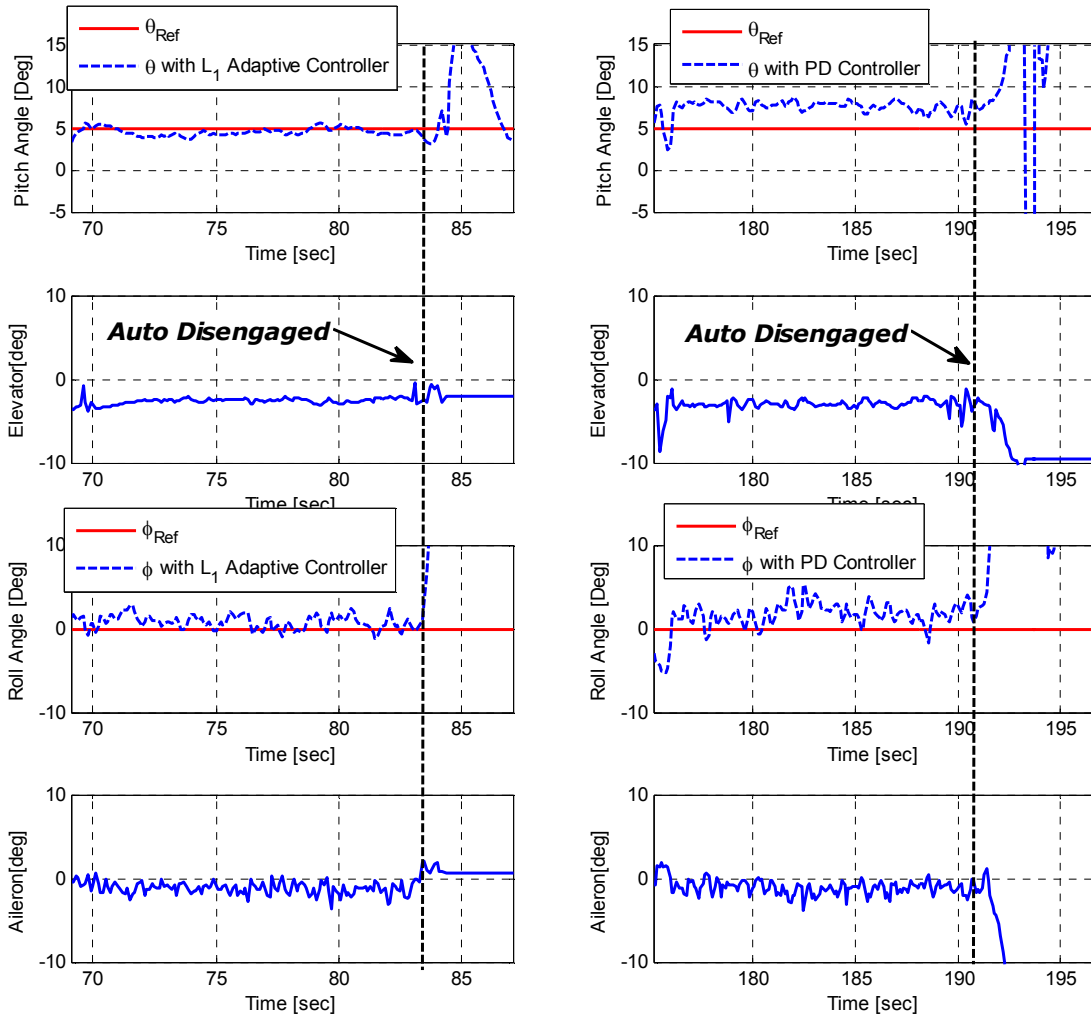

Figure 16. Longitudinal (top) and lateral (bottom) responses with $\mathcal{L}_1$ adaptive controller and PD controller

E. Autothrottle and Steering Control

The autothrottle for speed control is required for accurate take-off and landing. The controller includes an integrator term to compensate for the large time delay caused by the large time constant of the electric motor. It also has proportional feedback and feed-forward terms to compensate for altitude tracking error and velocity error, respectively. The autothrottle control law is given as

$$\delta_{thr} = K_{vt_{FB}} \Delta V_t + \int K_{ivt} \Delta V_t + K_{vt_{FF}} \Delta H_e \tag{25}$$

American Institute of Aeronautics and Astronautics
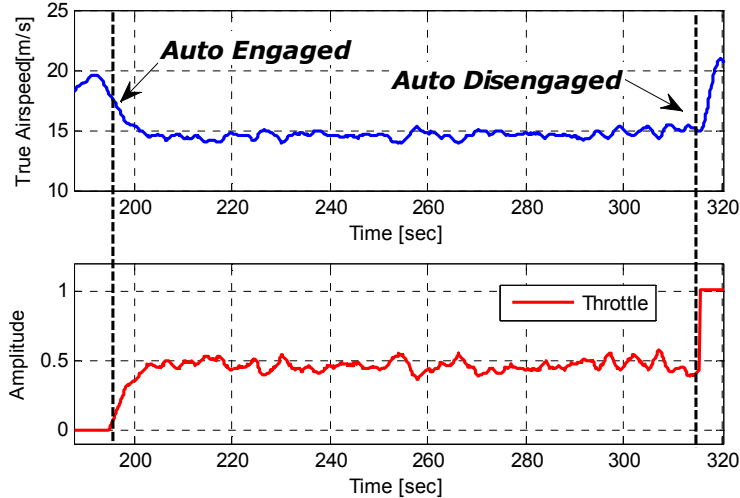
Figure 17. Velocity control history.

As can be seen in Figure 17, the controller can track a speed command of 15.0 m/s with error less than 0.5m/s.

Steering control assures that the vehicle accelerates to the take-off speed on a straight path on the runway without deviating from it. A PD control structure is chosen for steering so that yaw rate is fed back to reduce the yaw motion caused by the motor's anti-torque. The steering control is proportional to the difference between the runway direction angle and the horizontal flight path angle. Since the nose wheel steering and rudder control of the testbed UAV is linked together, the steering control law can be written as follows:

$$\delta_{steer\&rud} = K_{steer}(\psi_{path} - \psi_{course}) + K_r r \tag{26}$$
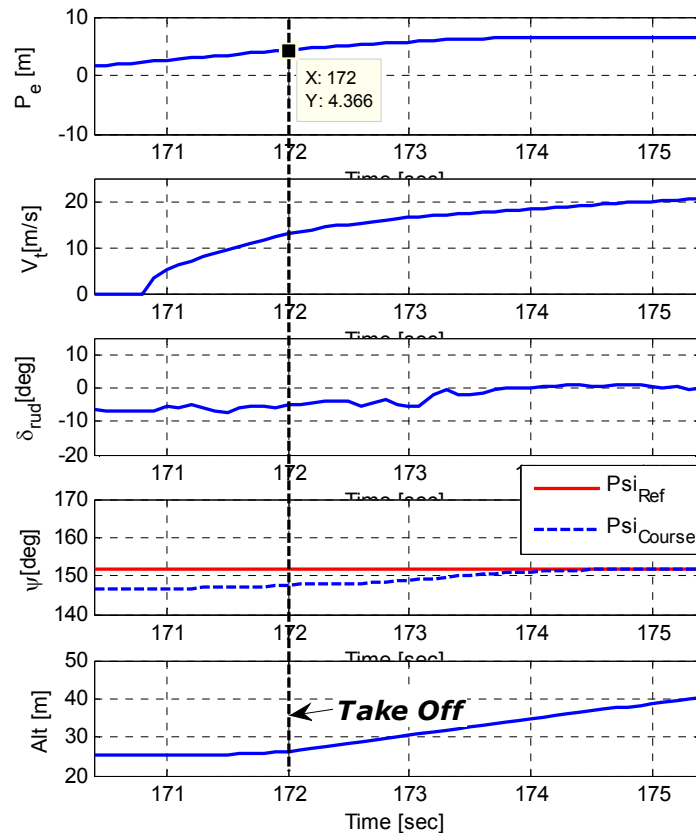
Figure 18. Steering control history

13
American Institute of Aeronautics and Astronautics

Eq. (26) enables the aircraft track the center line of runway by maintaining the same heading along the runway. Even if the heading angle is changed due to disturbances such as cross wind and the propeller's anti-torque, The steering controller prevents excessive steering control input to stabilize heading angle of taxiing vehicle by feeding back the yaw rate. As the velocity increases, the rate feedback control is activated only at high speed range inside the specified safety region(±5 meters in lateral direction with respect to center of runway) on the runway by using the scheduled gains K_{steer} and K_r based on the vehicle's speed. The flight test of the proposed steering control law is shown in Figure 18. As shown therein, the rudder and steering controls are both used keep the vehicle on the runway as it accelerates. In the experiment result, the horizontal error from the center line of the runway remains less than four meters until take-off.

III. Flight Experiments

A. Flight Experiment Scenario

A flight test scenario (Figure 19) was conceived such that the vehicle, initially aligned with the runway, performs take-off, fly over the carrier, starts the approach, and then performs landing on the TDP. One arresting wire(Figure 20) is installed about forty millimeters above the runway surface.
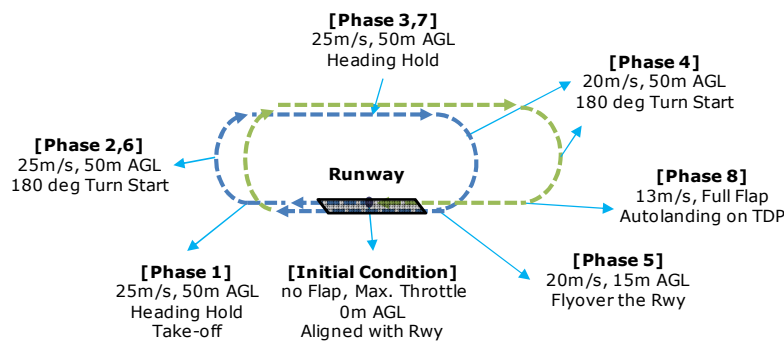

Figure 19. Circuit pattern flight scenario

Figure 20. Arresting wire on TDP

B. Operation logics and Emergency mode

One of the major components for automatic take-off and landing flight is the flight operation logic including emergency mode when the landing attempt fails.
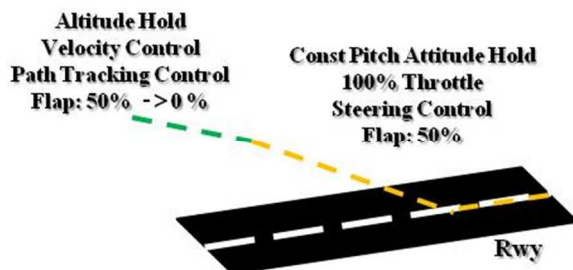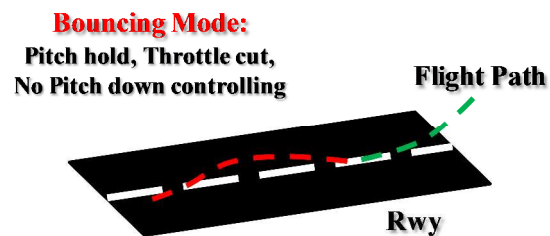

Figure 21. Take-off operations

Figure 22. Bouncing mode in landing

During the take-off phase, the pitch angel of the UAV should not exceed 10 degree to prevent tail-strike. The UAV is commanded to hold the pitch angle only since the altitude tracking is not yet important and the altitude measurement often has a large error from GPS. When the UAV accelerates from halt, it applies full throttle, 50 % of flap and active steering control. When it climbs up to 15 meters above ground level, the altitude tracking loop is activated. The reference pitch angle is set to be the current pitch angle to prevent any unnecessary control of elevator during acceleration. The reference roll angle is set to zero degree until the UAV reaches the take-off velocity. The deployed flap is retracted when the vehicle attains preset speed and altitude.

In landing phase, the vehicle decreases the speed and the flap is deployed when the speed drops below a prescribed point. The Recovery Decision Window(RDW) which is a decision point whether to land or not is located at fifty meters ahead of the TDP. When the vehicle did not pass the RDW, Go-Around mode is declared. The flare mode is activated at the flare altitude near the desired TDP to achieve minimizing the bouncing and landing gear shock. In addition, to reduce the bouncing of UAV, the pitching down control is deactivated and UAV is commanded to hold constant pitch angle when bouncing is occurred.
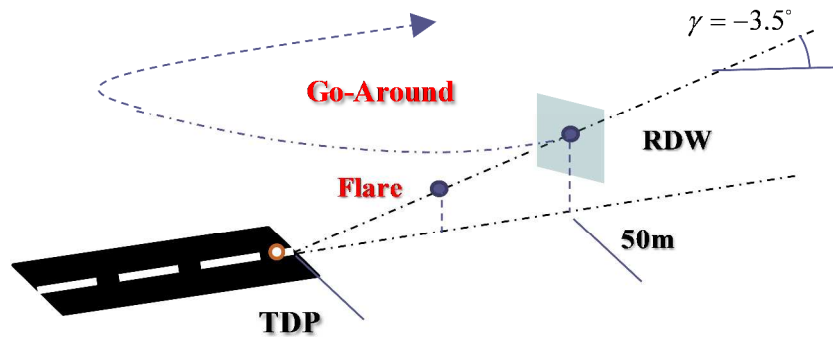

Figure 23. Landing operations with go-around mode

C. Flight Control System and PILS

A high fidelity real-time simulation environment is essential for aircraft control system design and development. Although there are a number of high-quality flight simulators available, some of those are quite limited to simulate complicated and varying flight conditions. For simulating automatic take-off and landing, some of the simulator have limited vehicle model so that some phenomena such as bouncing during landing, engine failure, taxiing on runway are not accurately simulated.

For developing automatic take-off and landing control system, we first developed PILS(Processor-In-the-Loop Simulation) using MATLAB/Simulink with an X-Plane simulator, which can be configured to transmit the vehicle states over UDP protocol in real time. The flight control computer receives vehicle data from X-Plane and sends calculated control commands over UDP. Then X-plane receives the control input and simulates the vehicle using it as the pilot's command from the joystick. The aforementioned algorithms and operational logics were tested and evaluated using the developed PILS before real flight experiment.


Figure 24. MATLAB/Simulink based PILS system using X-Plane

After validating the proposed algorithm, it is implemented on our in-house flight control system, which consists of an Inertial Measurement Unit (IMU), a DGPS receiver, a data communications modem, a flight control computer, with a servo control system, and a video transmission module as shown in Table 4.

Table 3. FCS specifications.

Components		Weight
CPU	PXA270 processor	30g
	600Mhz	
	RAM 128MB/Flash 32M	
	Linux 2.6	
Comm. Modem	MicroHard 900Mhz Modem	150g
IMU	Microstrain 3DM-GX3	50g
DGPS	Novatel OEM-V2-RT2 (including antenna)	300g
PWM Board	Custom PWM Board Input (7ch)/output(10ch) /Analog input(3ch)	20g
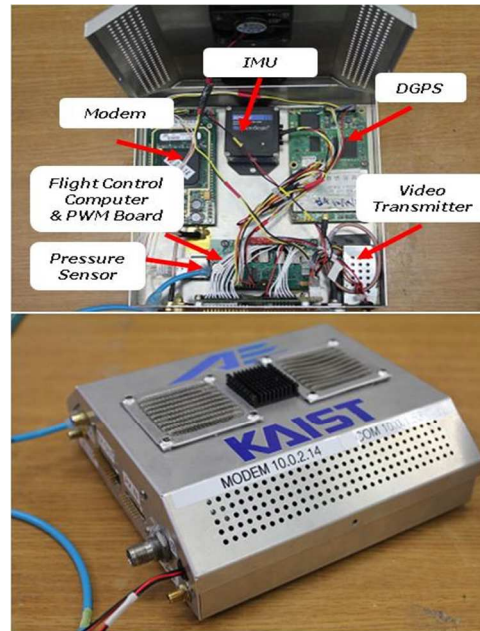
Figure 25. Flight Control Computer.

The navigation solution in the flight control software was obtained by a DGPS-aided INS using an extended Kalman filter (EKF) operated at 100Hz. This navigation system has an advantage of superior linear velocity and position tracking performance compared to the widely used AHRS(Attitude and Heading Reference System). In this research, a differential GPS from NovAtel was used in order to obtain higher-accuracy altitude as well as horizontal position measurement. The CPU board is built on a PXA270 600 MHz processor with 128 MB RAM and 32 MB Flash memory, which weighs only 30 grams but offers a significant computing power for sophisticated guidance, navigation and control algorithms presented in this paper. The autopilot runs custom flight control software, written in C++ running on Linux 2.6 kernel. PWM board provides various input/output ports for reading and generation PWM signals. Also, it is equipped with a differential pressure sensor calibrated using a wind tunnel test for estimating total airspeed.

D. Flight Test Result

In this section, the flight experiment result using the proposed algorithm is shown. Figure 26 and Figure 27 shows the entire flight trajectory of the UAV performing automatic take-off and landing in the proposed scenario.

In the automatic take-off step, after the take-off command was authorized, the flaps of the UAV were deployed to 50% position and began acceleration once the deployment was complete (Figure 28). As the aircraft begins to accelerate, the roll angle was fixed to zero degree and the current pitch angle was fixed until reaching the decision speed of 8 m/s. Once this decision speed is reached, the pitch angle is maintained at 10 degree and when the aircraft ascends to a certain altitude, the altitude tracking loop was activated. After the UAV ascends a certain altitude, the alignment process continues through roll angle control and the flaps are retracted. The result of the steering control was already shown in Figure 18, and Figure 29 displays the response of altitude, speed, and attitude angle during the automatic landing. As can be observed in the figure, stable landing performance was validated.

In the automatic landing stage, the UAV begins to decelerate as it approaches the runway. Since the UAV does not have spoilers, the flaps are deployed to reduce the speed while maintaining the lift. The flaps were designed to operate as a function of the landing approach speed, and during the landing the flaps are fully extended so that the UAV lands at a lowest speed. Near the TDP, a flare maneuver was performed to relieve the shock on the aircraft landing gears and the throttle was minimized for stable landing by reducing the elevation change rate. Figure 29

shows the aircraft response during the automatic landing sequence, where the altitude tracking error gradually reduced to reach within approximately 10cm of the TDP.
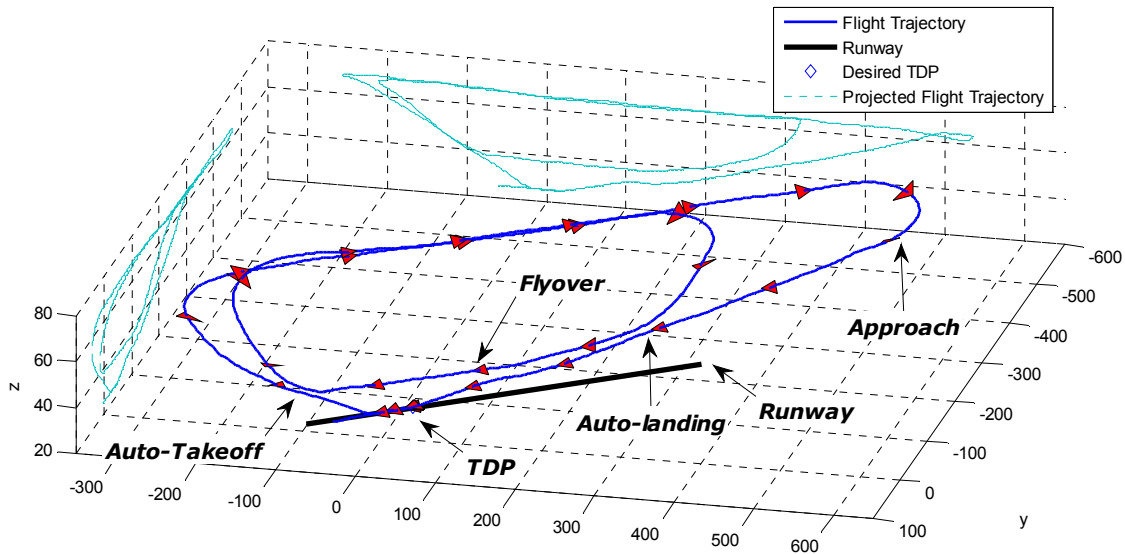

Figure 26. Automatic Takeoff and Landing Trajectory(3D)
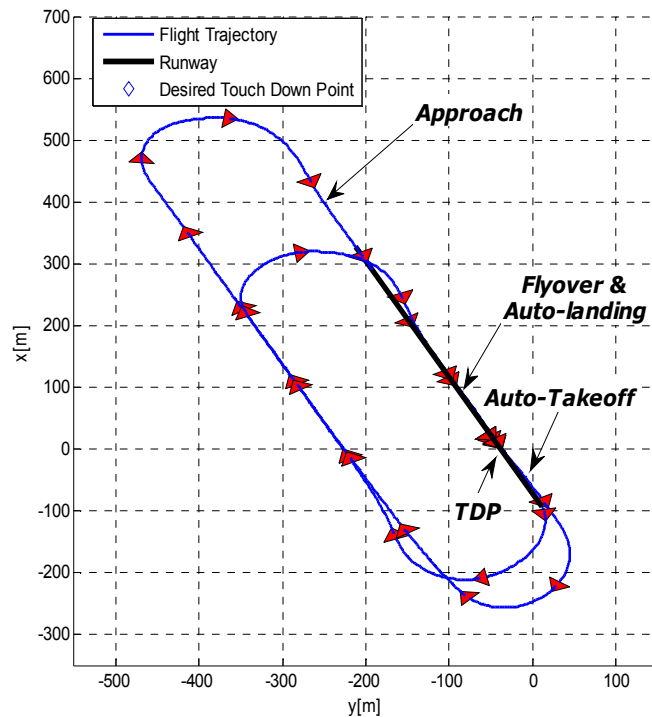

Figure 27. Automatic Takeoff and Landing Trajectory(2D)

Additional flight test is carried out to examine the performance of the proposed automatic take off and landing system on a realistic simulated carrier. The simulated carrier and arresting wire is shown in the left side of Figure 30. The simulated aircraft carrier deck landing area has an effective length of 30 meters, 8 meters wide and 0.8 meters above the ground. In the landing zone, there are 4 arresting wires with a distance of 4 meters between each other. The wires are connected to sandbag for damping of UAV landing speed.

The UAV started take off procedure on the ground runway beside the simulated carrier. The desired point is set to the second wire on the landing area. After the automatic take off, the UAV flew with the circuit pattern as shown

17

in Figure 27, it initially lined up with the carrier's runway during approach. Snapshots in Figure 30 show the view taken from the onboard camera during the final approach until just before the landing. In this experiment, the UAV's hook caught the third wire on the landing area. In the flight test, the longitudinal and the lateral guidance algorithms combined with the adaptive controller proposed in this study demonstrated a satisfactory performance in realistic operational environment.
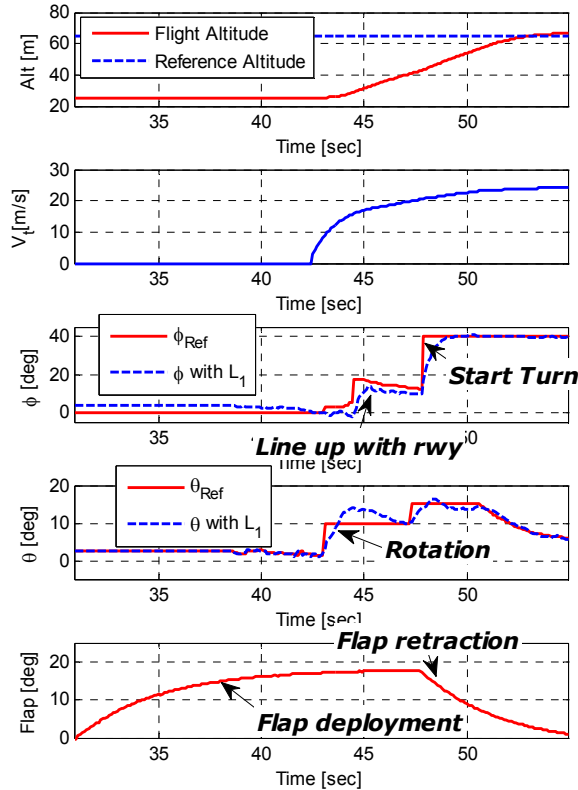

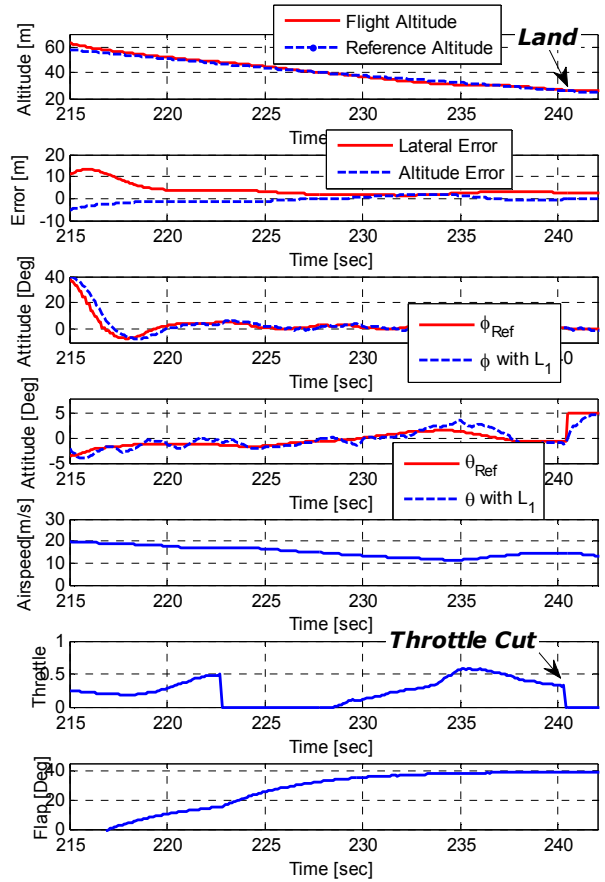**Figure 29. Automatic takeoff experiment**

Figure 28. Automatic landing experiment

Figure 30. Automatic takeoff and landing experiment on simulated aircraft carrier (a simulated carrier(left), landing scenes from onboard video (right))

18
American Institute of Aeronautics and Astronautics

IV. Conclusion

In this paper, in order to develop a high-precision automatic take-off and landing system, a comprehensive automatic take-off and landing system consisting of an inner loop attitude controller, longitudinal and lateral guidance algorithms, an $\mathcal{L}_1$ adaptive controller, velocity and steering controller, and automatic take-off and landing management logic is proposed. Since the adaptive control method proposed in this study does not require a separate gain scheduling for trim speed changes and flap deployment in the take-off and landing sequences, this method will help to shorten the development cycle of a new UAV.

For validation, an automatic take-off and landing scenario on runway with arresting wires for a fixed-wing UAV is employed, where the high-precision automatic take-off and landing capability is vital. Test results shows that the tracking error on TDP is within 2 m in the lateral direction and 10 cm in the longitudinal direction, which satisfies the automatic take-off and landing requirement for aircraft carrier-based operation.

Acknowledgments

References

[1] National Research Council, *Autonomous vehicles in support of naval operations*, National Academies Press, 2005.

[2] Williams, K. W., "A Summary of Unmanned Aircraft Accident/ Incident Data: Human Factors Implications," U.S. Department of Transportation Report No. DOT/FAA/ AM -04/24.

[3] Yun, S. J., Lim, J. S., Lee, Y. J., Ha, C. K. and Koo, H. J., "Automatic Landing Guidance Techniques of UAV," *ICASE Magazine*, Vol. 7, No. 5, 2001.

[4] Yun, D. H., Ki, C. D., "Simulation of Aircraft Automatic Landing using GPS," *Proceeding of the 12th KACC*, 1997.

[5] Cohenm, C. E., Cobb, H.S. and Lawrence , D. G., "Autolanding a 737 using GPS Integrity Beacons," *Journal of the Institute of Navigation*, Vol.42, No.3, 1995.

[6] Loegering, G., Harris, S., "Landing Dispersion Result - Global Hawk Auto-land System," *AIAA Technical Conference and Workshop on UAV*, Virginia AIAA 2002-3457, 2002.

[7] Prickett, A. L., Parkes, C. J., "Flight Testing of the F/A-18E/F Automatic Carrier Landing System*," Aerospace Conference, IEEE Proceedings*, Vol.5, pp2593-2612, 2001.

[8] Grohs, T., Fischer, B. , Heinzinger, O. and Brieger, O., "X-31 VECTOR - ESTOL to the Ground Flight Test Results and Lessons Learned," *AIAA Guidance, Navigation, and Control Conference and Exhibit*, Rhode Island, 2004.

[9] Fossen, T. I., *Marine Control Systems*, Marine Cybernetics, 2002.

[10] Dubins, L., "On curves of minimal length with a constraint on average curvature, and with predescribed initial and terminal positions and tangent,*" American Journal of Mathematics*, Vol.79, No.3, pp497-516, Jul. 1957.

[11] Tischler, M. B., Remple, R. K., *Aircraft and Rotorcraft System Identification Engineering Methods with Flight Test Examples*, American Institute of Aeronautics and Astronautics, Inc., Reston, Virginia.

[12] You, D. I., Shim, H. C., "System Identification and Controller Design of an Autonomous Fixed-Wing Micro Aerial Vehicle,"*2009 Fall KSAS Conference*, Korea. Nov. 2009.

[13] Xargay, E., Hovakimyan, N. and Cao, C., "Benchmark Problems of Adaptive Control Revisited by L1 Adaptive Control," *17th Mediterranean Conference on Control & Automation*, Thessaloniki, Greece, pp.31~36. 2009.

[14] Hovakimyan, N. and Cao, C., *L1 Adaptive Controller Theory Guaranteed Robustness with Fast Adaptation, Advances in Design and Control*, 2010.

[15] Cao, C. and Hovakimyan, N., "Stability Margins of L1 Adaptive Controller: Part II," *Proceedings of the 2007 American Control Conference* ,New York, July 2007, pp.3931-3936.